

CBET lolol

(Hopefully soon to be Dr.) Philip W. X. Moloney

IMPERIAL

June 2024

Submitted in partial fulfilment of the requirements for the degree of
Doctor of Philosophy of Imperial College London

Department of Physics
Imperial College London
Prince Consort Road
London SW7 2AZ

List of Acronyms

CBET Cross-Beam Energy Transfer

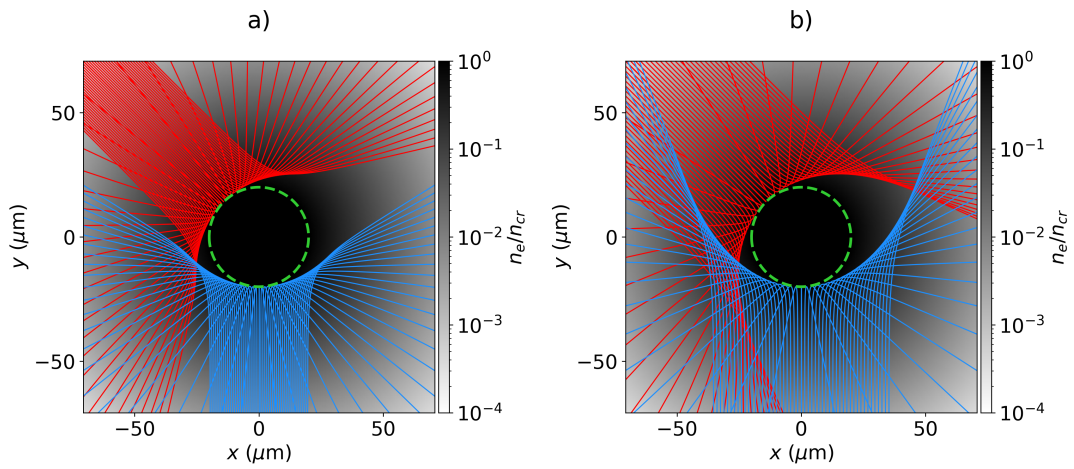


Figure 1.1: The trajectory of rays from two beams with Beam radii. The density profile for both simulations is $n_e = n_{cr} \exp [-(r_{\mu\text{m}} - 20)/100]$. Panels a) and b) plot rays from beams with widths $\sigma = 10$ μm respectively.

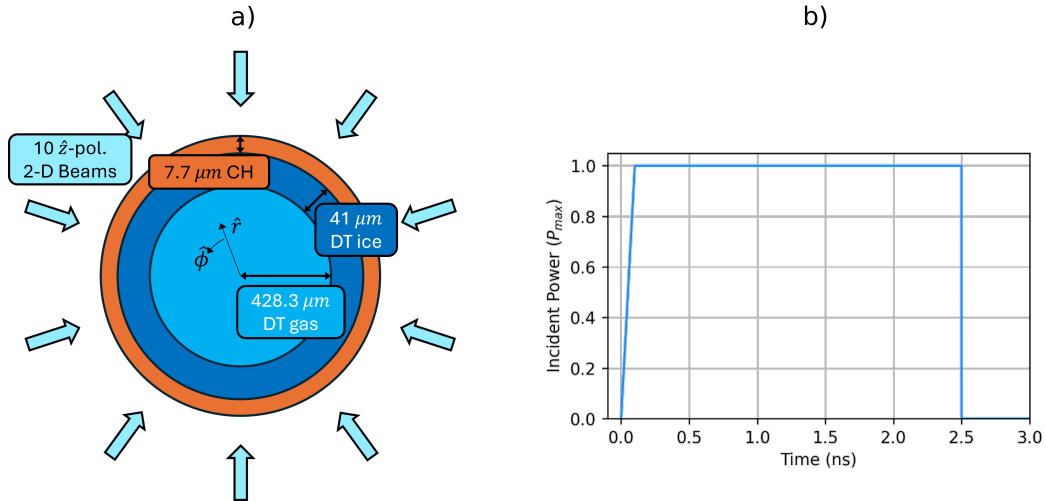


Figure 1.2: The target initial conditions with beam geometry, a), and pulse shape, b), used for the 2-D cylindrical simulations. All beams were polarised out of the simulation plane, in the $+\hat{z}$ direction. Initial layer radii were taken from the initial conditions for OMEGA shot 89224, presented in Fig. ??a.

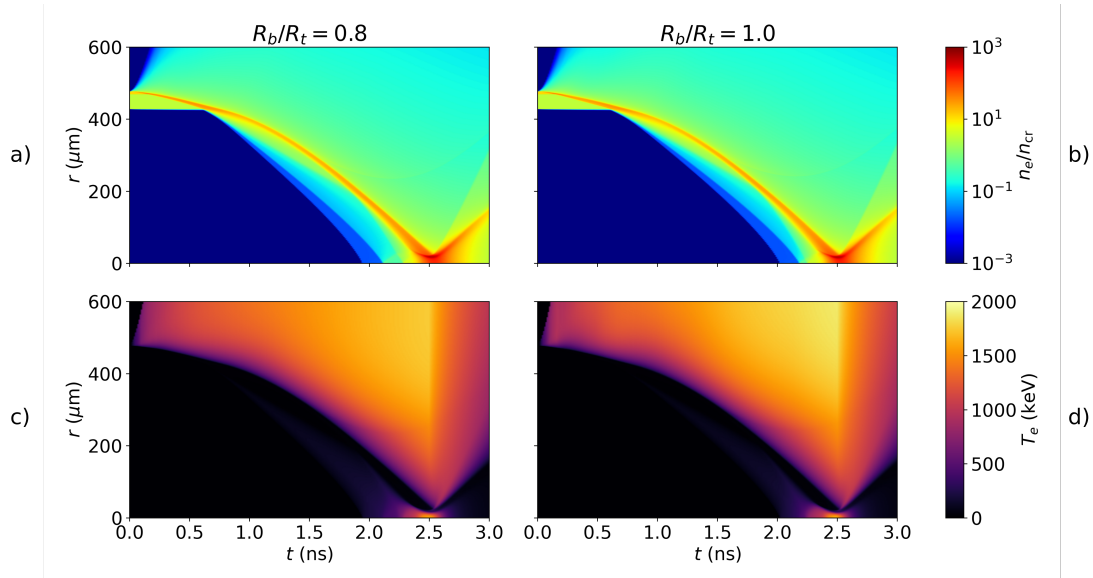


Figure 1.3: Streak plots from two of the 1-D tuning simulations. Panels a) & b) plot the electron density as a function of time (x -axis) and radius (y -axis) for the Cross-Beam Energy Transfer (CBET) simulations of the $R_b/R_t = 0.8$ & $R_b/R_t = 1.0$ simulations respectively. Panels c) & d) plot the same but electron temperature for the $R_b/R_t = 0.8$ & $R_b/R_t = 1.0$ simulations respectively.

1 Cylindrical Simulations to Study the Effect of Beam Radius in Direct-Drive

1.1 Introduction to Beam Radius in Direct-Drive Inertial Confinement Fusion

1.1.1 Statistical Modelling of OMEGA Direct-Drive Implosions

1.1.2 Beam Radius in Statistical Modelling

1.2 Cylindrical Simulation Platform for Beam Radius Parameter

Table 1.1: Results of the 1-D Tuning Simulations.

R_b/R_t		P_{\max} (TW/cm)	I_0 (10^{14} W/cm 2)	t_{bang} (ns)	Y_{DT} (10^{13} /cm)
0.75	No CBET	54.44	0.85	2.49	1.53
	CBET			2.51	1.44
0.80	No CBET	58.25	0.83	2.49	1.56
	CBET			2.51	1.45
0.85	No CBET	63.44	0.83	2.48	1.67
	CBET			2.51	1.43
0.90	No CBET	70.00	0.85	2.47	1.82
	CBET			2.50	1.41
0.95	No CBET	77.94	0.89	2.46	1.99
	CBET			2.49	1.49
1.00	No CBET	87.25	0.93	2.45	2.15
	CBET			2.49	1.60
1.05	No CBET	97.94	0.99	2.46	2.27
	CBET			2.50	1.61
1.10	No CBET	110.00	1.06	2.47	2.31
	CBET			2.51	1.52

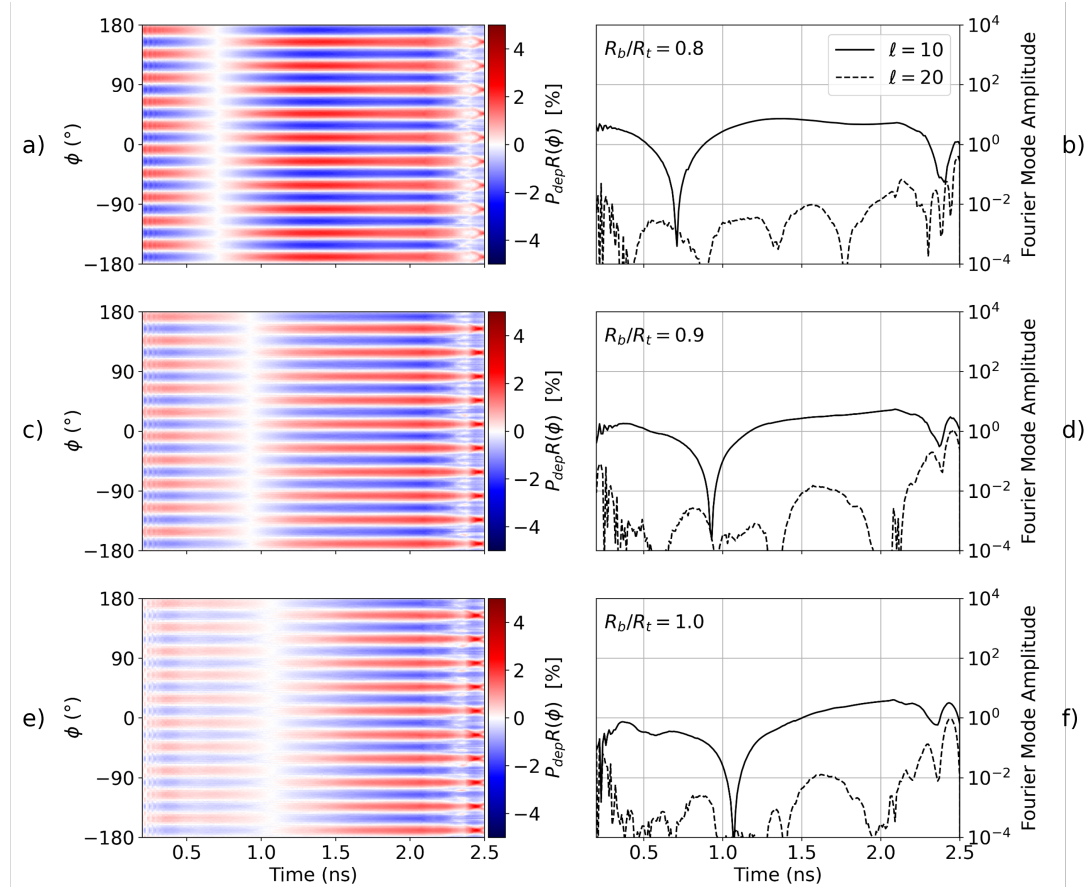


Figure 1.4: This figure plots the radially integrated deposited power from no CBET simulations as a function of time (x -axis) and angle (y -axis), alongside amplitudes of the dominant modes from a Fourier power spectrum. Panels a) and b) plot the radially integrated deposited power and Fourier modes respectively for the $R_b/R_t = 0.8$ simulation. The same is plotted for the $R_b/R_t = 0.9$ simulation in c) & d) and for the $R_b/R_t = 1.0$ simulation in e) & f). The mode 10 from the number of beams is clearly visible in the radially integrated power plots as 10 peaks to troughs in angle at a given time, *i.e.* 10 cyclical perturbations along a vertical lineout.

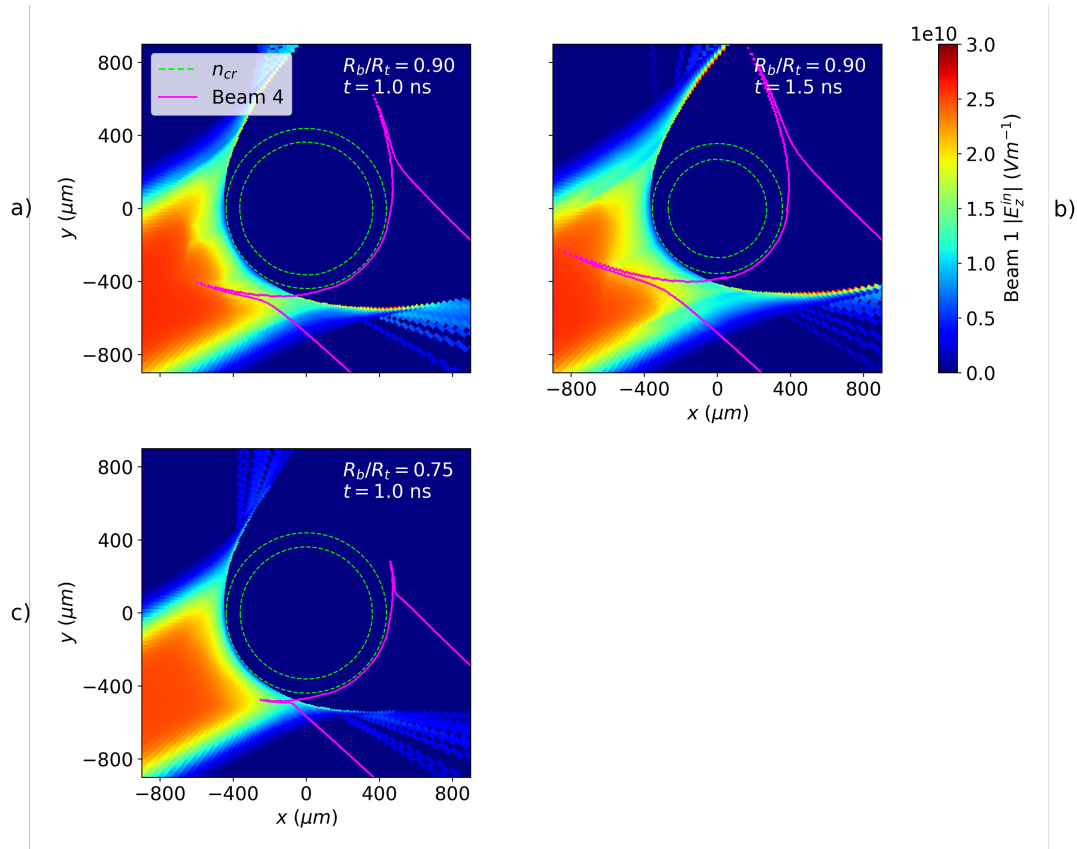


Figure 1.5: This plot illustrates the origin of the CBET induced asymmetry on power deposition and its dependence on R_b/R_t and target convergence. Each panel plots the incident field (including the effect of CBET), along with contours of the critical electron density and the $|E_z^{in}| = 1 \times 10^{10} \text{ Vm}^{-1}$ contour of another beam. Panel a) & b) plot this for the $R_b/R_t = 0.9$ simulation at $t = 1.0$ ns & $t = 1.5$ ns respectively. The convergence of the target in this time interval leads to greater convergence and therefore a change in the spatial location across the beam of the resonant CBET interaction. Panel c) plots the $R_b/R_t = 0.75$ at the same time as panel a). This demonstrates that the $R_b/R_t = 0.75$ beam is not wide enough at this time to lead to a resonant CBET interaction, unlike the wider beam in panel a).

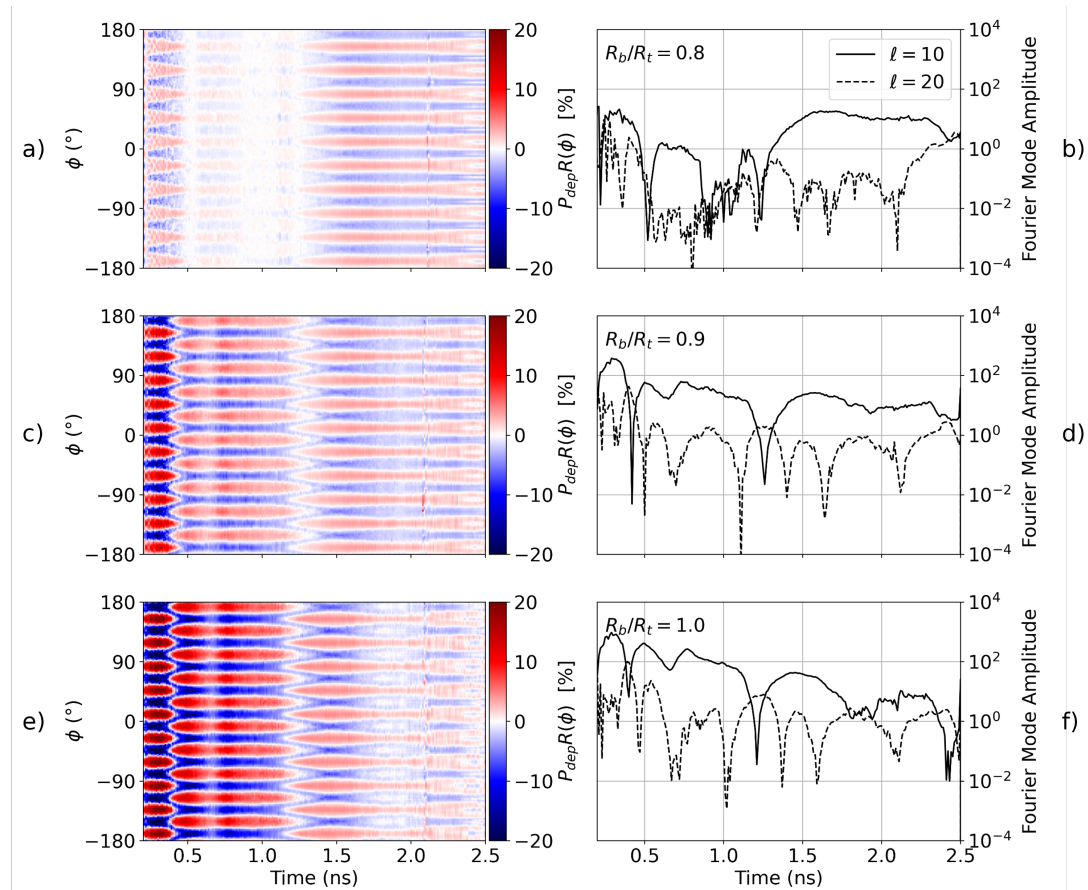


Figure 1.6: This figure plots the same as Fig. 1.4, but now for the equivalent simulation including the effect of CBET. Comparing these results and those in Fig. 1.4 demonstrates that CBET introduces additional modal-flips of the deposition and amplifies the magnitude of asymmetries.

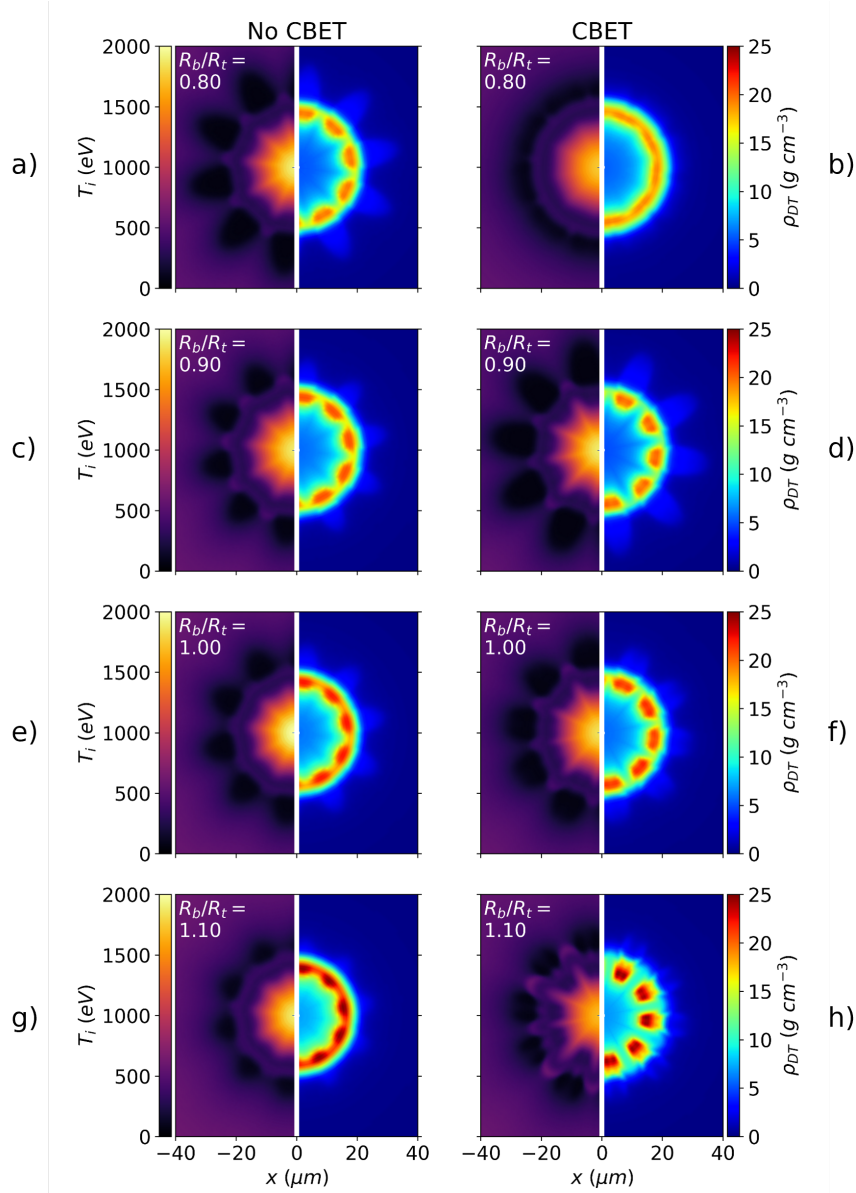


Figure 1.7: Densities of the DT fuel and ion temperatures for various R_b/R_t simulations both with and without CBET. Each row correspond to a different R_b/R_t value; the left column contains simulations without CBET; and the right column contains simulations with CBET. It is visible from the density plots that increasing R_b/R_t improves stagnation symmetry for the no CBET simulations, but degrades it for the CBET simulations.

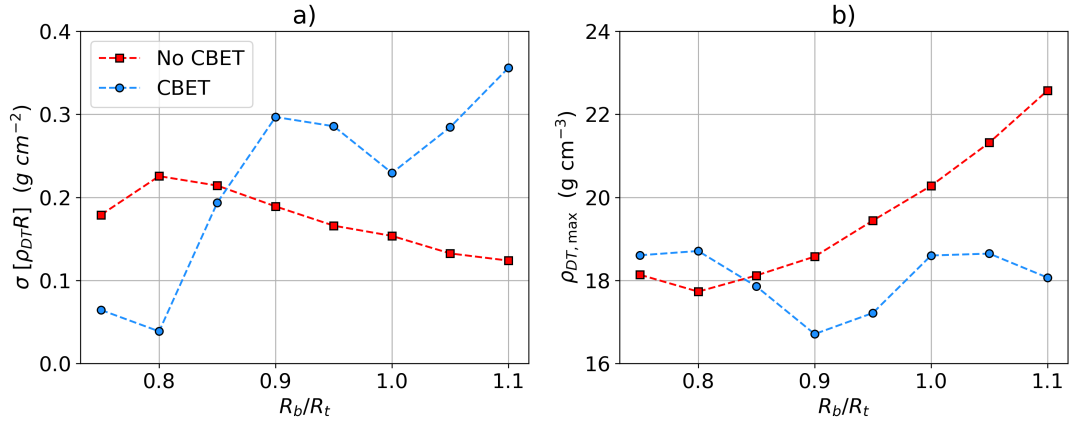


Figure 1.8: Trends of a) stagnation asymmetry and b) maximum (azimuthally averaged) fuel density for CBET and no CBET simulations. The no CBET improvement in symmetry with R_b/R_t is observed which also corresponds to improved compression. The symmetry trend including CBET is more complex, but broadly the stagnation state symmetry is worse with increasing R_b/R_t .

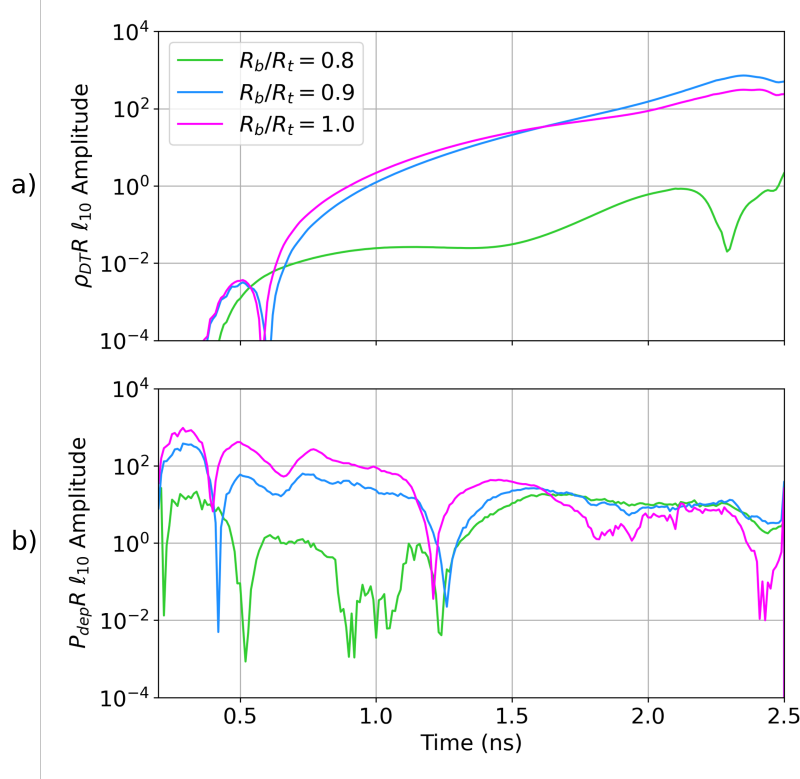


Figure 1.9: Time resolved $\ell = 10$ Fourier power spectrum amplitude for a) $\rho_{DT}R$ and b) $P_{dep}R$ for CBET simulations with 3 R_b/R_t values. The developing but unrealised modal flip for $R_b/R_t = 0.8$ from $t \sim 0.5 \rightarrow 1.2$ ns reduces the $P_{dep}R_{\ell=10}$ leading to slow $\rho_{DT}R_{\ell=10}$ growth and ultimately a relatively symmetric stagnation state. Despite large values of $\rho_{DT}R_{\ell=10}$ initially, the developing modal flip of the $R_b/R_t = 1.0$ simulation from $t \sim 1.8 \rightarrow 2.1$ ns slows the density asymmetry growth.

Appendices

A Numerics Appendices

Bibliography

Permissions